Supporting Information

High-performance artificially reeled silkworm silk via a multi-task and high-efficiency centrifugal reeling technique and its application in soft actuators

Teng Hou[a], Xianglong Li[a], Shu Liu[a], Jing Zhou[a], Yujing Bian[a], Lele Zhou[a], Mingbo Sun[a], Wenlong Zhou[ab], and Bin Yang[a]*

a. National Engineering Lab for Textile Fiber Materials and Processing Technology, College of Textile Science and Engineering (International Institute of Silk), Zhejiang Sci-Tech University, Hangzhou 310018, China.

b. Wenzhou University of Technology, Wenzhou 325035, China.

Supporting information contains:

Fig. S1-S13

Table S1-S5

Movie S1-S11

Fig. S1 Traditional silk processing technology.

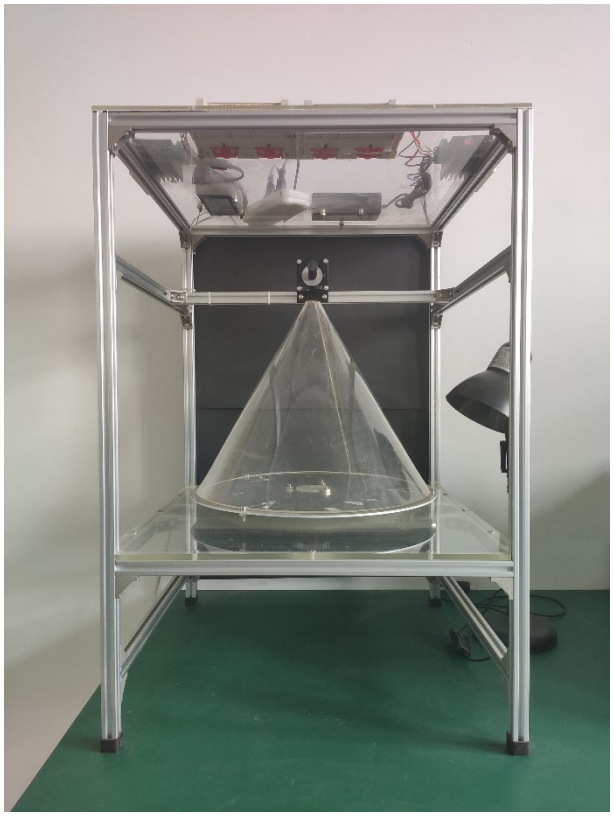

Fig. S2 Centrifugal reeling device.

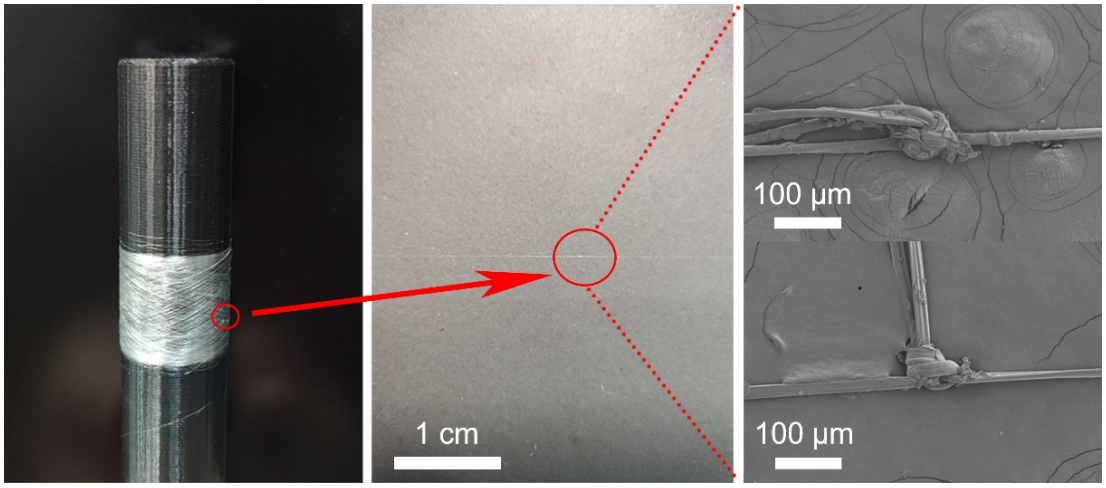

Fig. S3 Photographs and SEM images of the knots on CRSs.

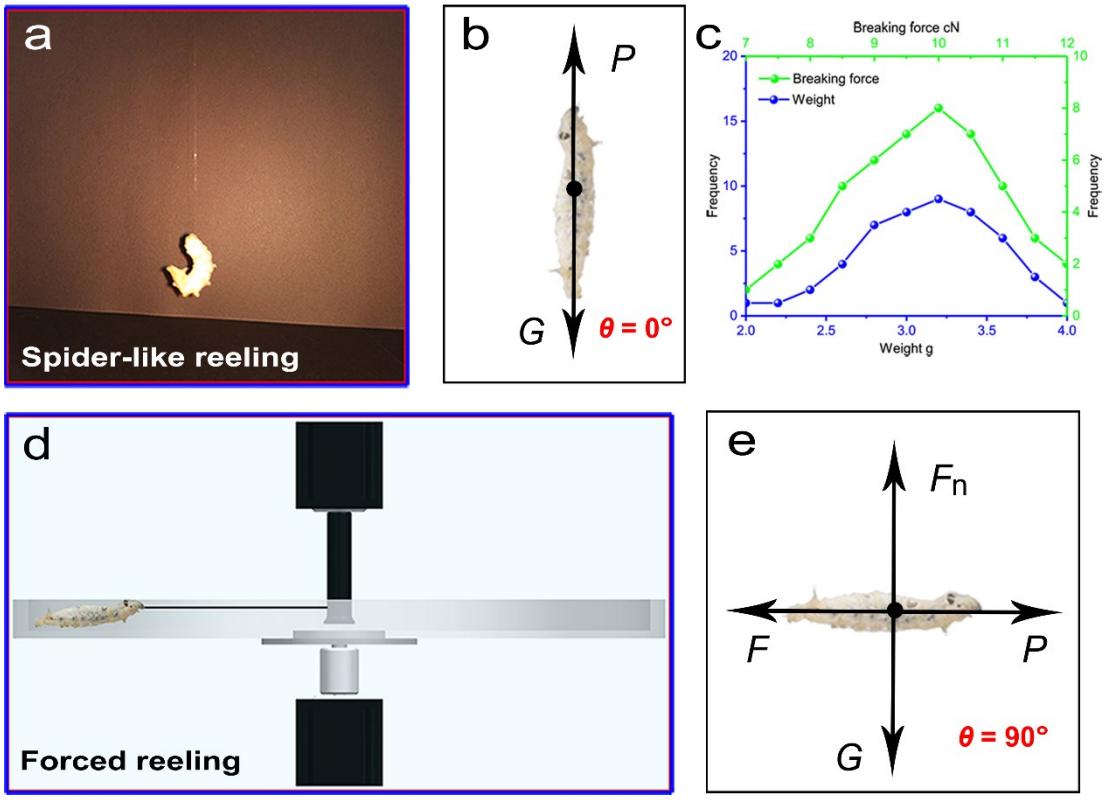

Fig. S4 a) Spider-like reeling: a photograph of a dangling spinning silkworm when $\theta = 0°$. b) Force analysis of spider-like reeling. c) Distributions of the breaking force and the weight of 50 samples (p(Forece) = 0.5058, p(Weight) = 0.9409, $p > 0.05$, normal distribution, Shapiro-Wilk normality test). d) Forced reeling: a diagram of a spinning silkworm on the aclinic rotating aluminium plate when $\theta = 90°$. e) Force analysis of forced reeling.

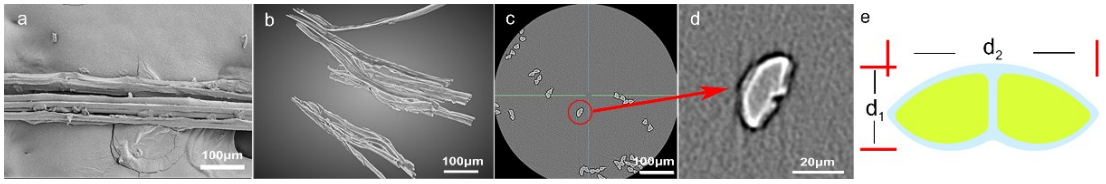

Fig. S5 SEM image (a), 3D morphology (b), cross-sectional images (c; d) and cross-sectional diagram (e) of cocoon silk (CS, d_1 and d_2 indicate the minor diameter and the major diameter of cocoon silk, respectively).

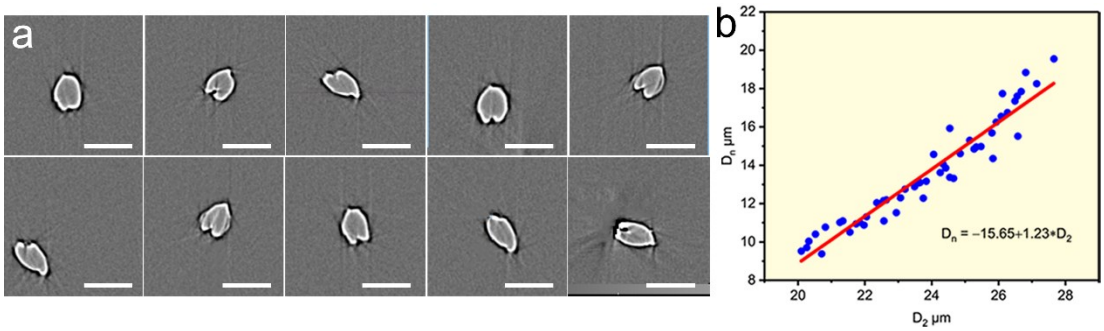

Fig. S6 a) Cross-sectional SEM images of CRSs (V_1 = 60 mm s^{-1}; V_2 = 30 rpm; T_1 = 1 s; T_2 = 2 s, scale bar: 30 μm). b) Relationship between the nominal diameter (D_n) and D_2 of CRSs, D_n is the diameter of the equivalent circle of the fibre cross-sectional area, where the data were measured at different locations along fibre axis every 0.5 m from at least ten silkworms (R^2 = 0.9224, p(D_2) = 0.1129, p(D_n) = 0.1183, p > 0.05, normal distribution).

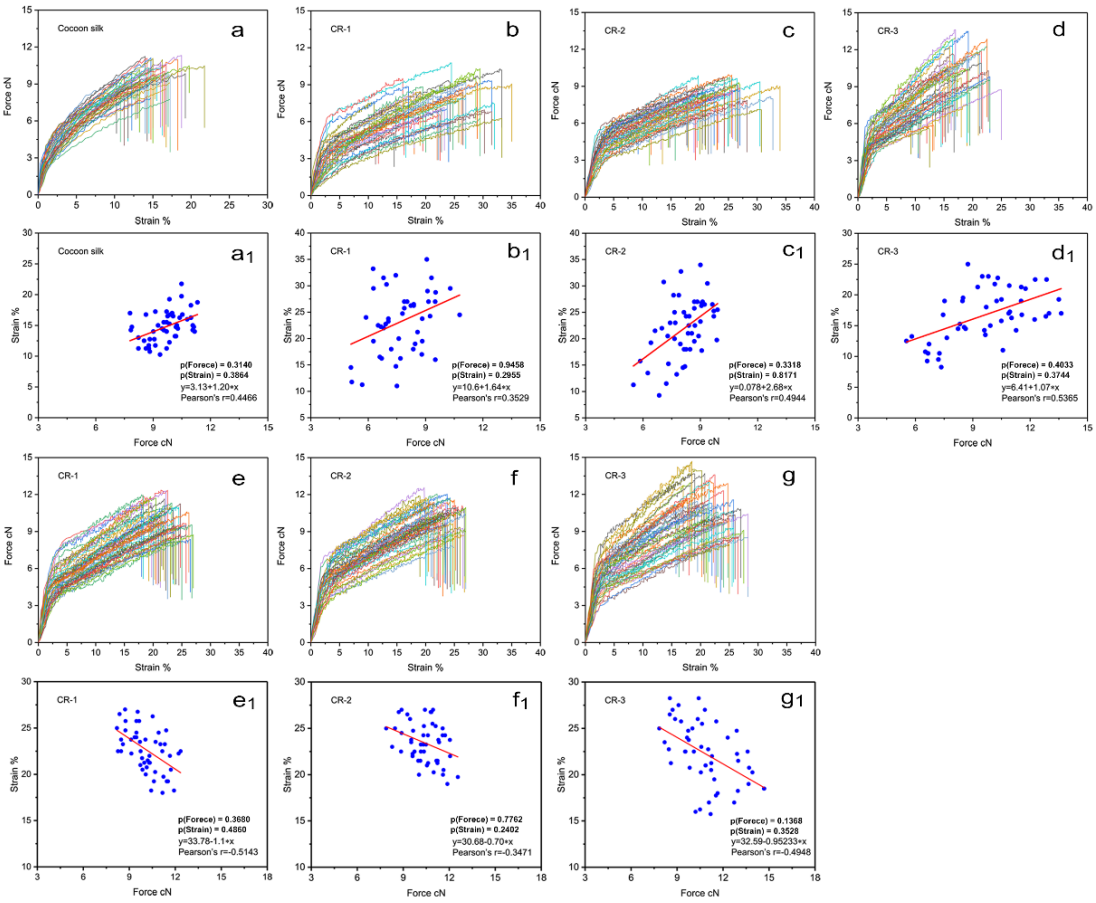

Fig. S7 The breaking force-strain curves, the distributions of breaking force and strain and the corresponding correlations of 50 randomly selected samples. a; a_1) CS, b; b_1) CR-1: V_1 = 10 mm s^{-1}; V_2 = 0 rpm; T_1 = 1, 2, 3, …, n s; T_2 = 0 s, c; c_1) CR-2: V_1 = 10 mm s^{-1}; V_2 = 0 rpm; T_1 = 6 s; T_2 = 2 s, d; d_1) CR-3: V_1 = 10 mm s^{-1}; V_2 = 30 rpm; T_1 = 6 s; T_2 = 2 s, e; e_1) CR-1: V_1 = 60 mm s^{-1}; V_2 = 0 rpm; T_1 = 1, 2, 3, …, n s; T_2 = 0 s, f; f_1) CR-2: V_1 = 60 mm s^{-1}; V_2 = 0 rpm; T_1 = 1 s; T_2 = 2 s, g; g_1) CR-3: V_1 = 60 mm s^{-1}; V_2 = 30 rpm; T_1 = 1 s; T_2 = 2 s (all the breaking force and breaking strain distributions obey normal distribution).

The correlation of breaking force and breaking strain of CRS obtained under different reeling types and reeling speeds (low speed: 10 mm s^{-1} and high speed: 60 mm s^{-1}) were analyzed to give further insights into the effect of centrifugal reeling on mechanical properties. The Pearson's r (representing

the correlation of breaking force and breaking strain) of CS, CRS-1, CRS-2, and CRS-3 was 0.45, 0.35, 0.49, and 0.54 for low speed, respectively, and -0.51, -0.35, and -0.49 for CRS-1, CRS-2, and CRS-3 for high speed, respectively. It is clear that high reeling speed causes a negative correlation, which is consistent with the previous works, while CRS shows a positive correlation at low reeling speed. According to a reported study, the extensional flow of liquid crystal nanofibrils in the silk duct orientates their molecules and draws them together before the stiff plates, initiating the removal of the water shell around the hydrophobic fibroin and hence initiating silk II (β-crystallites) formation.[1] In the case of CRS, the nascent fibrils enter the constriction between the stiff plates and are stretched under the combinative effects of different reeling speeds, rotational speeds and reeling-break step instead of the natural spinning speed, leading to further extensional flow, water removal, and molecular orientation, resulting in highly-oriented and well-refined β-crystallites. The correlation analysis indicates that the CRSs with highly-oriented and well-refined β-crystallites and highly oriented nascent fibrils obtained at high reeling speed are difficult to stretch in latter tensile test, showing the increase of breaking stress and the decrease of breaking strain with the reeling speed increasing; while the stretching induced by reeling-break step or rotational step has slight effects on improving the microstructures of CRSs.

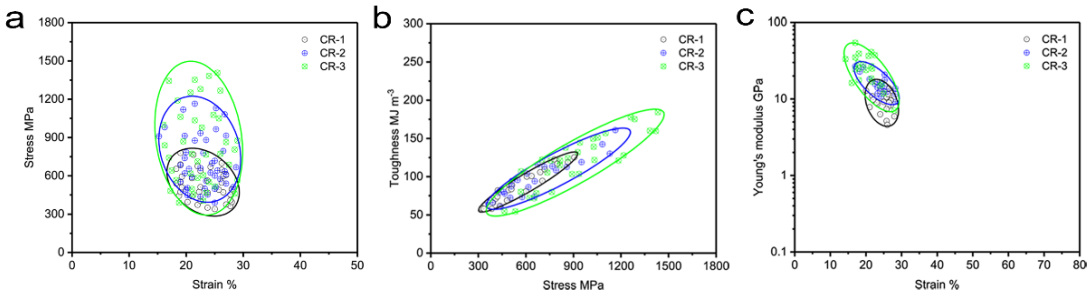

Fig. S8 Mechanical characteristic diagrams of breaking stress versus breaking strain (a), toughness versus breaking stress (b), and Young's modulus versus breaking strain (c) of CRSs obtained from different reeling types and reeling conditions (CR-1: V_1 = 60 mm s^{-1}; V_2 = 0 rpm; T_1 = 1, 2, 3, …, n s; T_2 = 0 s, CR-2: V_1 = 60 mm s^{-1}; V_2 = 0 rpm; T_1 = 1 s; T_2 = 2 s, CR-3: V_1 = 60 mm s^{-1}; V_2 = 30 rpm; T_1 = 1 s; T_2 = 2 s).

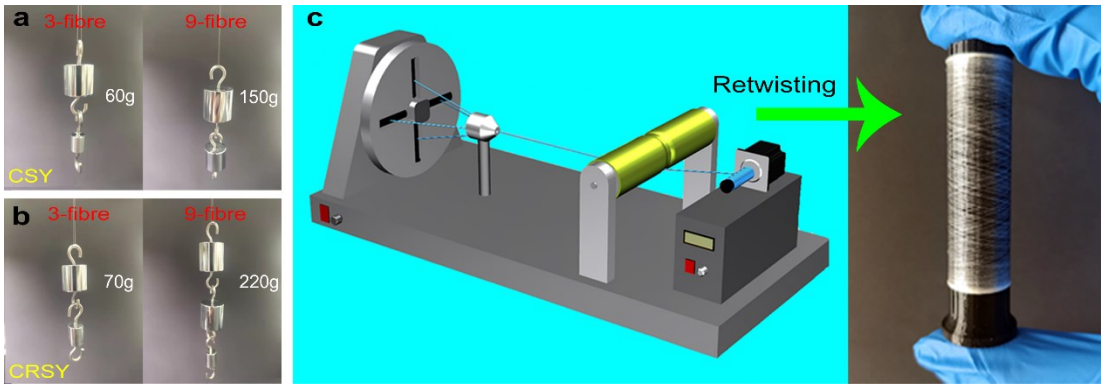

Fig. S9 a) A 3-fibre twisted cocoon silk yarn (CSY) with the length of 10 cm can hold up a 60 g weight without breaking (left photograph); a 9-fibre twisted CSY with the length of 10 cm can hold up a 150 g weight without breaking (right photograph), $T_m = 25$. b) A 3-fibre twisted CRSY with the length of 10 cm can hold up a 70 g weight without breaking(left photograph); a 9-fibre twisted CRSY with the length of 10 cm can hold up a 220 g weight without breaking (right photograph), $T_m = 25$. c) Schematic illustration of the twister and the resulting silk yarns.

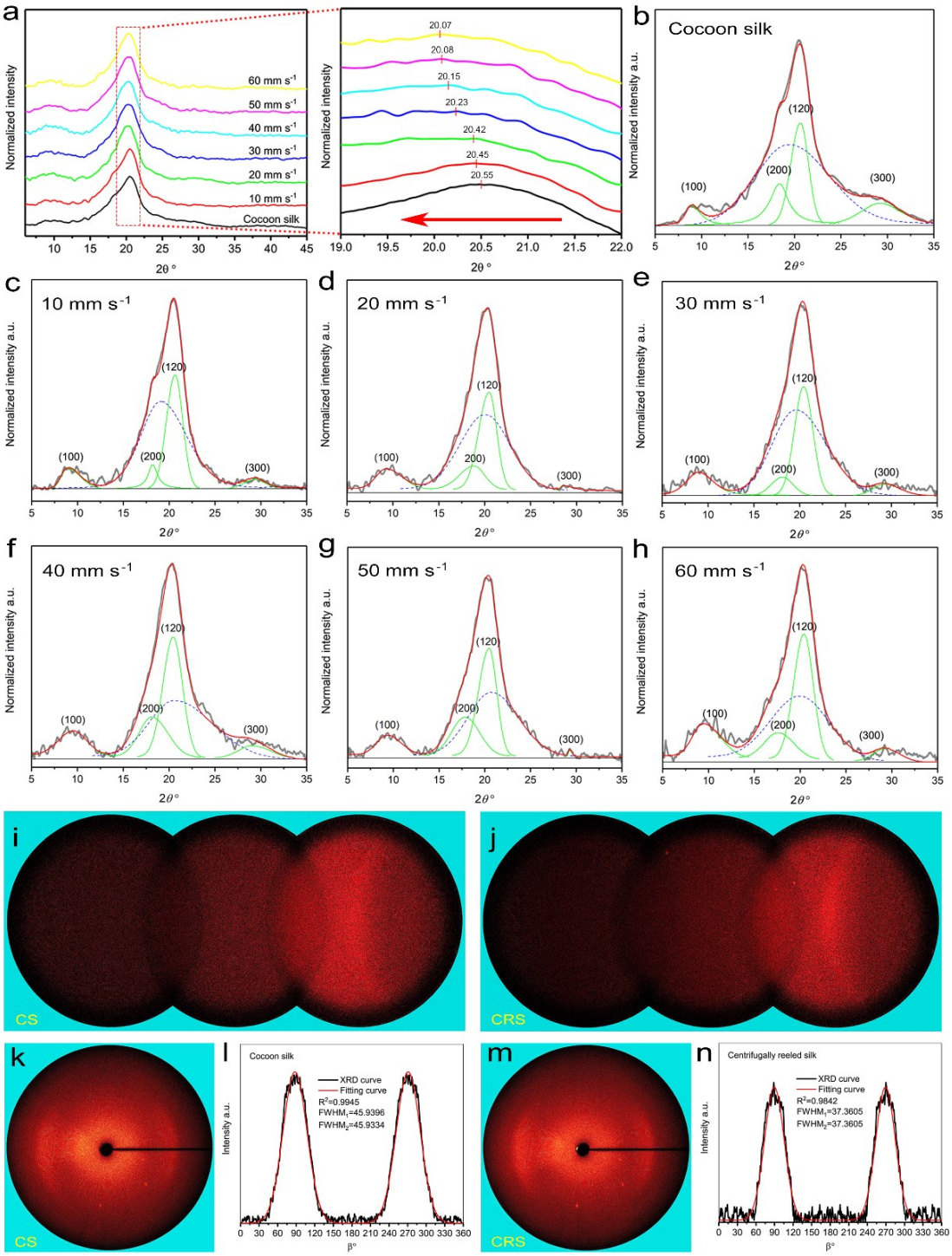

Fig. S10 a) XRD curves of CS and CRS (V_1 = 10, 20, 30, 40, 50, 60 mm s^{-1}, V_2 = 30 rpm; $T_1 = C/V_1$ s; T_2 = 2 s). b-h) The radial integration of intensity as a function of diffraction angle 2θ along the equatorial direction of the WAXD pattern of CS and CRS reeled at 10-60 mm s^{-1} in CR-3. For silkworm silk, the equatorial data was deconvoluted into four crystalline peaks corresponding to the (100), (200), (120) and (300) Bragg reflections (green, solid line) and an amorphous

halo (blue, dashed line). i; j) Two-dimensional crystalline diffractive patterns of CS and CRS. k, m) Two-dimensional patterns of CS and CRS. l, n) One-dimensional intensity distribution profiles and the deconvolution of the intensity distribution profiles of CS and CRS.

Wide-Angle X-ray Diffraction (WAXD). A two-dimensional wide-Angle X-ray diffraction was employed to characterize the crystallinity, crystallite size, and crystalline orientation. The crystallinity (X_c), crystallite size (D_c), and crystalline orientation (f_c) were calculated as follows:[2]

$$X_c = \frac{\sum I_c}{\sum I_c + \sum I_a} \tag{S1}$$

$$D_c = \frac{\kappa\lambda}{\beta cos\theta} \tag{S2}$$

$$f_c = \frac{360 - \sum h_i}{360} \tag{S3}$$

Where I_c represents the crystallite intensity, I_a refers to amorphous integral intensity, κ is the Scherrer constant (κ = 0.9), β means the full width as half-maximum of corresponding peak at the diffraction angle θ, and h_i is the full width at half-maximum (FWHM) of crystal peaks in orientation.

Crystallinity and size: The crystallinity is determined by the ratio of the under area of crystalline peaks to that of the total reflection patterns in equatorial data. The radial integration of intensity as a function of diffraction angle along the equatorial direction of the WAXD pattern was deconvoluted into crystalline peaks and amorphous halo (Fig. S10b-h). The crystallite sizes along *a* and *b* directions are determined by the position and β of the (200) and (120) peaks.

Orientation: the variation of definition and brightness of signal from Fig. S10k and m is in agreement with the diffraction crystalline images (Fig. S10i and j). DIFFRAC.EVA software was used to integrate the pattern from 0° to 360° to obtain the one-dimensional profiles through the circular integral method, as shown in Fig. S10l and n.

The number of the crystallite (n_β) within the cross-section of the nanofibril was estimated by the following equation:[3]

$$n_\beta = \frac{\pi {d_f}^2}{3\sqrt{3}{l_\perp}^2} \tag{S4}$$

Where d_f is the diameter of the nanofibrils and $l_\perp = \frac{\sqrt{ab}}{c\%^{\frac{1}{3}}}$ is the inter-crystallite distance in the transverse direction, where c% represents the crystallinity of the silk fibre. *a* is the length of L_a, and *b* is the length of L_b. n_β denotes the width of a network, and the crystalline structure results were listed

in Table S4 and S5.

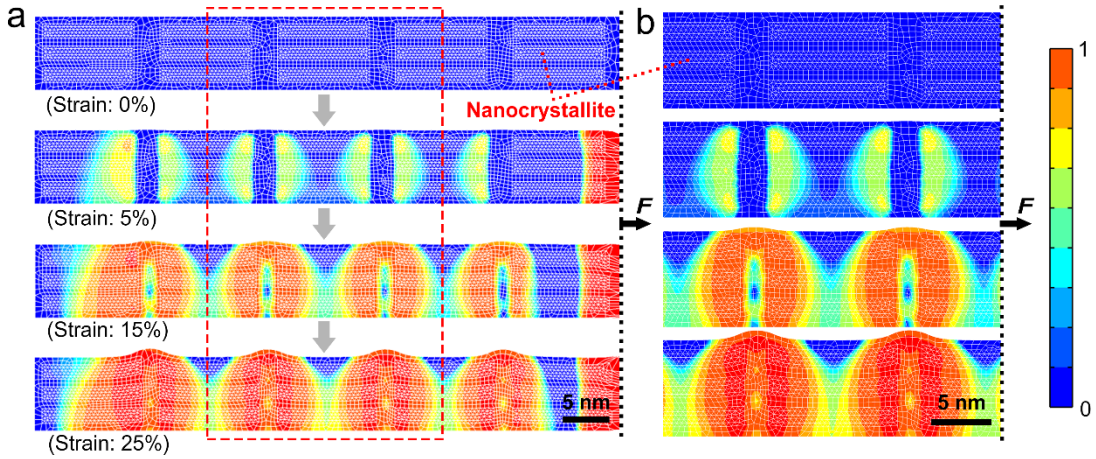

Fig. S11 Snapshots of finite elemental simulation of the nanofibril of CRS under stretching deformation (nanocrystallite size: 2 × 3 × 10 nm). a) The stress distribution of a nanofibril with a strain of 25%. b) The stress distribution around the nanocrystrallites with a strain of 25%.

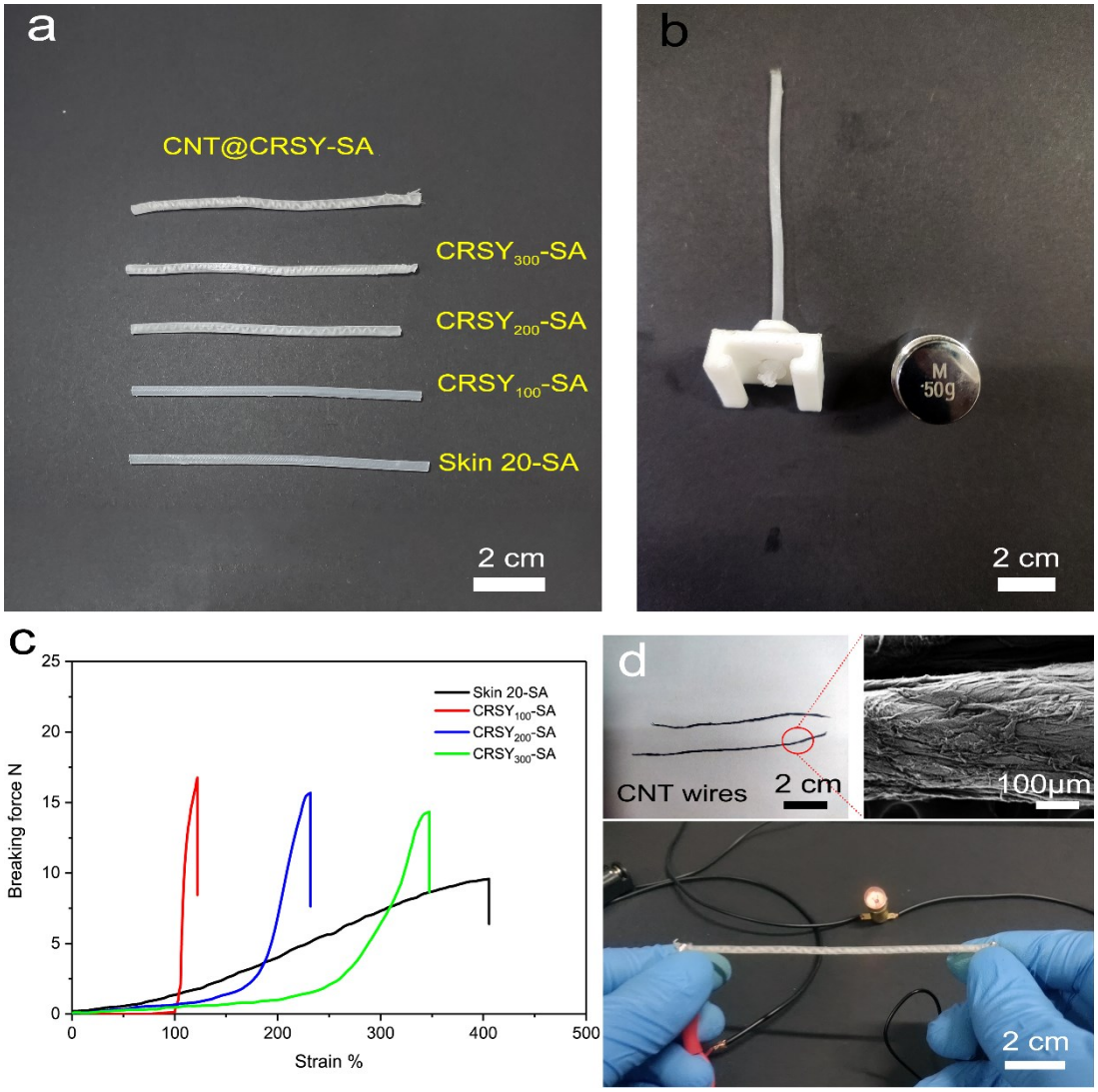

Fig. S12 a) Photographs of the CRSY-SAs. b) A photograph showing the 3D printed supporter for connecting the SA and the loading weight. c) Breaking force-strain curves of the CRSY-SAs. d) Photograph and SEM image of the CNT wires,

and the stretching conductivity of CNT@CRSY-SA.

Device for the small bulb lighting test comprised a 1.5 V bulb and wires with croc clips purchased from a local hardware store. The real-time resistance of the CNT@CRSY-SA under deformations of stretching and twisting were measured by a digital multimeter (03005, SATA Tools, China). The resistances were average values of 3 times at every position recorded according to of stretching and twisting gradients.

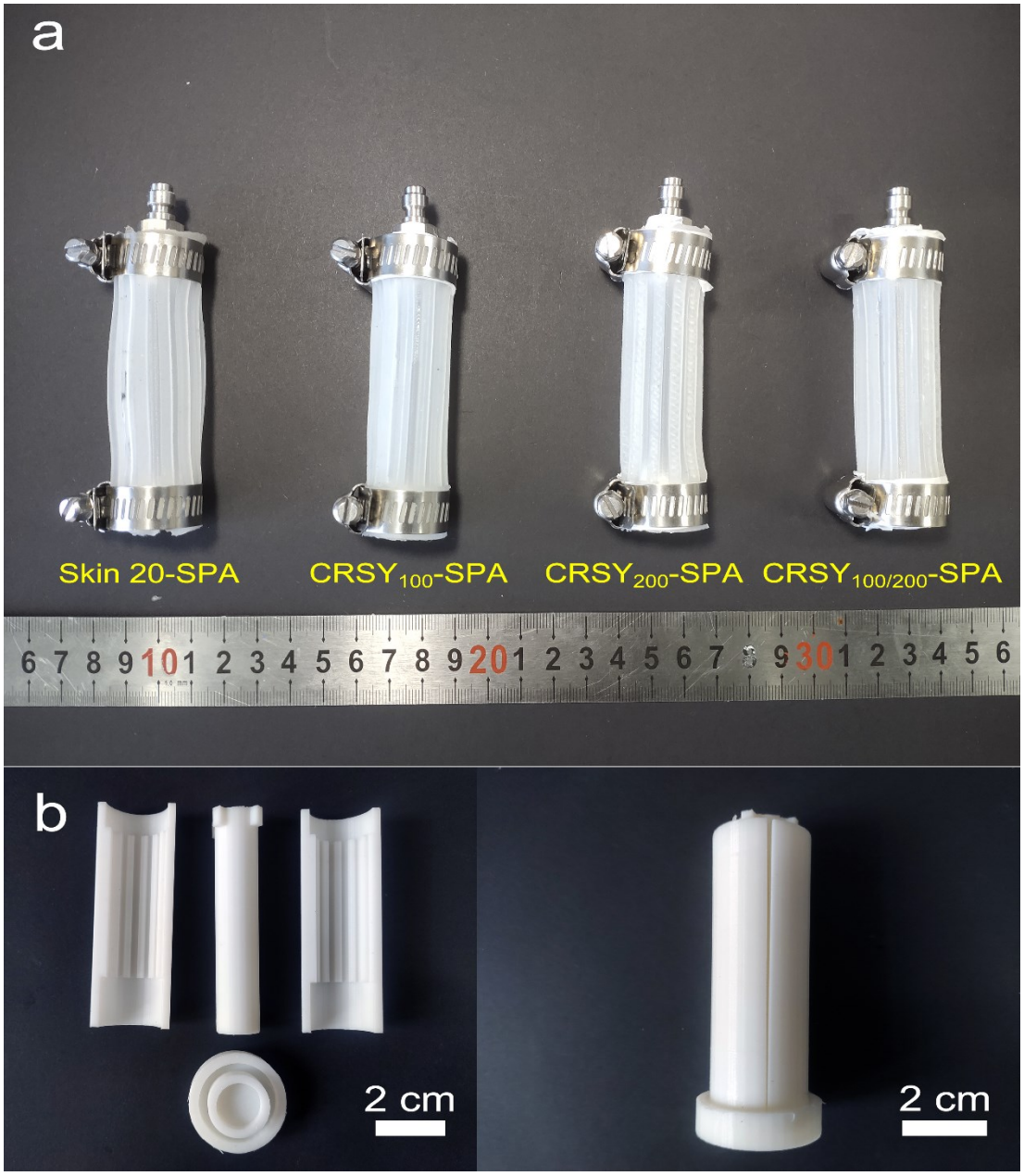

Fig. S13 a) SPAs enhanced by CRSYs with different lengths and allocations. b) Photographs of the 3D printed mould for the fabrication of SPAs (the SPA motions were inflated by a vacuum pressure pump, SCJ-10, Subo Instrument Co. Ltd., China).

Table S1 Nominal diameter (μm) and reeling length (m) of CRSs reeled at speeds of 10-60 mm s^{-1}.

	Silk type	10 mm s^{-1}	20 mm s^{-1}	30 mm s^{-1}	40 mm s^{-1}	50 mm s^{-1}	60 mm s^{-1}
Nominal diameter (μm)	CRS-1	20.88±1.97	20.09±1.87	18.09±1.3	17.43±1.71	17.13±2.74	16.01±1.7
	CRS-2	20.02±1.95	18.65±1.26	17.19±1.55	16.35±1.6	15.31±1.9	14.32±1.21
	CRS-3	18.32±2.04	17.43±1.44	16.59±1.55	15.29±1.89	14.11±2.21	13.62±2.68
Reeling length (m)	CRS-1	31.65±10.41	16±6.88	13.84±2.57	10.35±5	8.05±4.01	3.9±2.4
	CRS-2	139±44.31	56.7±16.99	46.2±15.03	31.85±14.29	17.4±6.06	26.56±7.2
	CRS-3	97.09±33.72	44.08±15.61	35.8±17.75	25.44±11.48	14.52±7.63	21.15±11.55
	Forced reeling	44.73±32.75	14.54±4.22	6.25±4.57	0.86±0.38	0.55±0.18	0.46±0.1

(CR-2: $T_1 = C/V_1$ s; T_2 = 2 s, CR-3: V_2 = 30 rpm; $T_1 = C/V_1$ s; T_2 = 2 s)

Table S2 Breaking strain, breaking force and breaking stress of CS and CRSs.

Mechanical property	Silk type	Mean value	Maximum value	Minimum value	Standard deviation
Breaking strain/%	CS	14.76	21.75	10.25	2.54
	CRS-1	22.64	27	18	2.36
	CRS-2	23.43	27	19	2.15
	CRS-3	22.22	28.25	15.75	3.38
Breaking force/cN	CS	9.65	11.32	7.79	0.94
	CRS-1	10.11	12.35	8.26	1.1
	CRS-2	10.38	12.56	8.7	1.07
	CRS-3	10.88	14.68	7.84	1.75
Breaking stress/MPa	CS	234.26	497.51	147.96	71.19
	CRS-1	525.27	779.19	339.29	120.43
	CRS-2	702.38	1164.87	412.34	205.9
	CRS-3	844.83	1447.85	389.1	319.48

(CR-1: V_1 = 60 mm s^{-1}; CR-2: V_1=60 mm s^{-1}, T_1 = 1 s, T_2 = 2 s; CR-3: V_1 = 60 mm s^{-1}, V_2 = 30 rpm T_1 = 1 s, T_2 = 2 s)

Table S3 Mechanical properties of typical materials.

Materials	Stress/MPa	Strain/%	Modules/GPa	Toughness/MJm^{-3}	References
Cotton	280-820	3-10	5.5-12.6	10-23	[4-9]
Wool	162-249	32-48	1.75-4.5	44-65	[10-13]
Spider silk	838-1495	18-37.5	5.5-19.85	87-256	[14-16]
Forced reeled silk	360-967	11.5-34	11.65-22.4	40-155	[17-21]
Cocoon silk	242-721	14-25	5-16.3	20.5-98	[22-31]

Table S4 Crystalline structural parameters of CRS-3 reeled at speeds of 10-60 mm s^{-1} (Batch 1).

	Sample	CRS-3 10 mm s^{-1}	CRS-3 20 mm s^{-1}	CRS-3 30 mm s^{-1}	CRS-3 40 mm s^{-1}	CRS-3 50 mm s^{-1}	CRS-3 60 mm s^{-1}
L_b	2θ °	20.64	20.47	20.43	20.37	20.32	20.30
	FWHM °	2.05	2.41	2.43	2.45	2.50	2.56
	d Å	4.30	4.34	4.34	4.36	4.37	4.37
	Crystallite nm	3.90	3.32	3.29	3.26	3.20	3.12
L_a	2θ °	18.59	18.53	18.13	18.09	18.07	17.93
	FWHM °	2.80	3.10	3.33	3.53	3.65	3.70
	d Å	4.77	4.76	4.89	4.90	4.91	4.94
	Crystallite nm	2.85	2.57	2.39	2.26	2.18	2.15
	Crystallinity %	43.80	45.13	50.68	52.27	57.16	58.95
	Residual error of fit %	6.39	7.88	7.04	10.04	8.85	10.26

(V_2 = 30 rpm; T_1 = 1 s; T_2 = 2 s)

Table S5 Crystalline structural parameters of CS and CRSs obtained from 3 batches.

Sample	Direction	Crystal structure parameter	CS	CRS-1 60 mm s^{-1}	CRS-2 60 mm s^{-1}	CRS-3 60 mm s^{-1}
Batch 1	L_b	2θ °	20.67	20.33	20.32	20.30
		FWHM °	2.03	2.65	2.62	2.56
		d Å	4.29	4.36	4.37	4.37
		Crystallite nm	3.94	3.02	3.05	3.12
	L_a	2θ °	18.62	18.09	18.09	17.93
		FWHM °	2.79	3.77	3.72	3.70
		d Å	4.76	4.90	4.90	4.94
		Crystallite nm	2.86	2.11	2.14	2.15
		n_β	48.61	99.97	97.24	106.01
		Crystallinity %	42.73	53.34	53.18	58.95
		Residual error of fit %	7.60	7.36	4.43	10.26
Batch 2	L_b	2θ °	20.63	20.33	20.31	20.26
		FWHM °	2.00	2.59	2.62	2.60
		d Å	4.30	4.37	4.37	4.38
		Crystallite nm	4.00	3.09	3.05	3.07
	L_a	2θ °	18.75	18.03	18.04	17.89
		FWHM °	2.25	3.50	3.72	3.47
		d Å	4.73	4.92	4.91	4.95
		Crystallite nm	3.54	2.28	2.14	2.29
		n_β	37.60	89.87	97.32	96.83
		Crystallinity %	40.87	52.88	53.24	59.09
		Residual error of fit %	9.34	8.40	6.57	6.68
Batch 3	L_b	2θ °	20.64	20.30	20.28	20.31
		FWHM °	2.13	2.49	2.56	2.57
		d Å	4.30	4.37	4.38	4.37
		Crystallite nm	3.75	3.21	3.12	3.12
	L_a	2θ °	18.45	18.01	17.94	17.90
		FWHM °	2.58	3.25	3.61	3.46
		d Å	4.80	4.92	4.94	4.95
		Crystallite nm	3.09	2.45	2.21	2.30
		n_β	47.75	79.16	93.84	93.25
		Crystallinity %	43.22	51.66	54.73	57.57
		Residual error of fit %	5.38	7.41	5.76	8.62

(CR-1: V_1 = 60 mm s^{-1}; V_2 = 0 rpm; T_1 = 1, 2, 3, …, n s, CR-2: V_1 = 60 mm s^{-1}; V_2 = 0 rpm; T_1 = 1 s; T_2 = 2 s, CR-3: V_1 = 60 mm s^{-1}; V_2 = 30 rpm; T_1 = 1 s; T_2 = 2 s)

Movie S1: The working process of CR-1.

Movie S2: The working process of CR-2.

Movie S3: The working process of CR-3.

Movie S4: The spinning silkworm keeps a stable dangling state at reeling speed of 10 mm s^{-1}.

Movie S5: Three spinning silkworms are reeling synchronously to prepare CRSY.

Movie S6: The stress distribution of a nanofibril under 25% stretching deformation.

Movie S7: The working processes of CS and CRSYs based microactuators (White: CS, Black: CRSY, Blue: $CRSY_{wet}$, Gray: $CRSY_{50}$).

Movie S8: The rotation recovery performances of Skin 20-SA and $CRSY_{200}$-SA.

Movie S9: The CNT@CRSY-SA maintains stable conductivity.

Movie S10: The CRSY-SPAs shows controllable inflating motions with or without load (1 kg).

Movie S11: The inflating and deflating processes of Skin 20-SPA.

References

1. T. Asakura, K. Umemura, Y. Nakazawa, H. Hirose and D. Knight, *Biomarcomoleculars*, 2007, **8**, 7.
2. J. Ma, L. Yu, S. Chen, W. Chen, Y. Wang, S. Guang, X. Zhang, W. Lu, Y. Wang and J. Bao, *Macromolecules*, 2018, **52**, 565-574.
3. G. Xu, L. Gong, Z. Yang and X. Y. Liu, *Soft Matter*, 2014, **10**, 2116-2123.
4. A. N. Netravali and S. Chabba, *Mater. Today*, 2003, **6**, 22-29.
5. M. J. John and R. D. Anandjiwala, *Polym. Compos.*, 2008, **29**, 187-207.
6. J. Biagiotti, D. Puglia and J. M. Kenny, *J. Nat. Fibers*, 2004, **1**, 37-68.
7. M. Li, Y. Pu, V. M. Thomas, C. G. Yoo, S. Ozcan, Y. Deng, K. Nelson and A. J. Ragauskas, *Composites, Part B*, 2020, **200**, 108254.
8. D. B. Dittenber and H. V. S. GangaRao, *Composites, Part A*, 2012, **43**, 1419-1429.
9. Z. Dong, X. Hou, I. Haigler and Y. Yang, *J. Cleaner Prod.*, 2016, **139**, 267-276.
10. N. V. Patil and A. N. Netravali, *ACS Omega*, 2019, **4**, 5392-5401.
11. C. Liu, C. Xie and X. Liu, *J. Nat. Fibers*, 2017, **15**, 162-173.
12. H. Barani, A. Haji and H. Maleki, *Int. J. Biol. Macromol.*, 2018, **108**, 585-590.
13. H. Liu, L. Zhao, G. Zhang, F. Pan and W. Yu, *Text. Res. J.*, 2020, **91**, 496-507.
14. J. L. Yarger, B. R. Cherry and V. Arjan, *Nat. Rev. Mater.*, 2018, **3**, 18008.
15. J. Pérez ln igueiro, M. Elices, J. Llorca and C. Viney, *J. Appl. Polym. Sci.*, 2001, **82**, 7.
16. L. Cheng, J. Shao, F. Wang, Z. Li and F. Dai, *Mater. Des.*, 2020, **195**, 108988.
17. Z. Shao and F. Vollrath, *Nature*, 2002, **418**, 741.
18. B. Mortimer, C. Holland and F. Vollrath, *Biomacromolecules*, 2013, **14**, 3653-3659.
19. M. M. Khan, H. Morikawa, Y. Gotoh, M. Miura, Z. Ming, Y. Sato and M. Iwasa, *Int. J. Biol. Macromol.*, 2008, **42**, 264-270.
20. S. Lin, Z. Wang, X. Chen, J. Ren and S. Ling, *Adv. Sci.*, 2020, **7**, 1902743.
21. Y. Wang, J. Ren, Z. Lv, L. Cao, S. Lin, Y. Pei, Q. Zhang, Z. Shao and S. Ling, *Chem. Eng. J.*, 2022, **435**, 134901.
22. C. Vepari and D. L. Kaplan, *Prog. Polym. Sci.*, 2007, **32**, 991-1007.
23. X. Fang, T. Wyatt, J. Wu and D. Yao, *Fibers Polym.*, 2016, **16**, 2609-2616.
24. X. Li, Q. Fan, Q. Zhang, S. Yan and R. You, *CrystEngComm*, 2020, **22**, 3884-3890.
25. J. Asrar and J. C. Hill, *J. Appl. Polym. Sci.*, 2002, **83**, 457-483.
26. C. Fu, Z. Shao and V. Fritz, *Chem Commun (Camb)*, 2009, DOI: 10.1039/b911049f, 6515-6529.
27. Z. Zhou, S. Zhang, Y. Cao, B. Marelli, X. Xia and T. H. Tao, *Adv. Mater.*, 2018, **30**, 1706983.
28. N. Ramos, M. S. Miranda, A. R. Franco, S. S. Silva, J. Azevedo, I. R. Dias, R. L. Reis, C. Viegas and M. E. Gomes, *ACS Sustainable Chem. Eng.*, 2020, **8**, 11872-11887.
29. L. Hu, Y. Han, S. Ling, Y. Huang, J. Yao, Z. Shao and X. Chen, *ACS Biomater. Sci. Eng.*, 2020, **6**, 1874-1879.
30. K. Yang, J. Guan, Z. Shao and R. O. Ritchie, *J. Mech. Behav. Biomed. Mater.*, 2020, **110**, 103942.
31. S. Chen, M. Liu, H. Huang, L. Cheng and H.-P. Zhao, *Mater. Des.*, 2019, **181**, 108077.